

## TEMPORAL EVOLUTION OF FREE MAGNETIC ENERGY ASSOCIATED WITH FOUR X-CLASS FLARES

JU JING<sup>1</sup>, P. F. CHEN<sup>2</sup>, THOMAS WIEGELMANN<sup>3</sup>, YAN XU<sup>1</sup>, SUNG-HONG PARK<sup>1</sup>, AND HAIMIN WANG<sup>1</sup>

<sup>1</sup> Space Weather Research Laboratory, New Jersey Institute of Technology, Newark, NJ 07102, USA; [jj4@njit.edu](mailto:jj4@njit.edu), [haimin@flare.njit.edu](mailto:haimin@flare.njit.edu),  
[yx2@njit.edu](mailto:yx2@njit.edu), [sp295@njit.edu](mailto:sp295@njit.edu)

<sup>2</sup> Department of Astronomy, Nanjing University, Nanjing 210093, China; [chenpf@nju.edu.cn](mailto:chenpf@nju.edu.cn)

<sup>3</sup> Max Planck Institut für Sonnensystemforschung (MPS), Max-Planck-Strasse 2, 37191 Katlenburg-Lindau, Germany; [wiegelmann@linmpi.mpg.de](mailto:wiegelmann@linmpi.mpg.de)

Received 2008 December 10; accepted 2009 January 30; published 2009 April 13

### ABSTRACT

We study the temporal variation of free magnetic energy  $E_{\text{free}}$  around the time of four X-class flares. The high-cadence photospheric vector magnetograms obtained by the digital vector magnetograph system at the Big Bear Solar Observatory are used as the boundary conditions to reconstruct the three-dimensional nonlinear force-free (NLFF) coronal field. In order to remove the effect of the net Lorentz force and torque acting in the photosphere, the vector magnetograms are preprocessed using the method devised by Wiegelmann et al.. Then a well-tested multigrid-like optimization code by Wiegelmann is applied to the preprocessed boundary data to extrapolate the NLFF coronal field with which we are able to estimate the free energy  $E_{\text{free}}$ . In all the four events, we find a significant drop of  $E_{\text{free}}$  starting  $\sim 15$  minutes before the peak time of the associated nonthermal flare emission, although long-term trend varies from event to event. We discuss the physical implication of the result, i.e., the magnetic relaxation is already going on in the corona well before the flare reconnection.

*Key words:* Sun: activity – Sun: corona – Sun: flares – Sun: magnetic fields

### 1. INTRODUCTION

It is widely believed that the coronal magnetic field provides energy for much of the solar activity such as flares and coronal mass ejections (CMEs; see, for review, Priest & Forbes 2002). Knowledge of the amount of free magnetic energy (i.e., magnetic energy that is available in a coronal magnetic configuration for conversion into kinetic and/or thermal energy) and its temporal variation associated with CMEs/flares would help our quantitative understanding of solar explosive phenomena. However, such studies have been rare and difficult due to both observational limitations and intrinsic physical problems.

Since the coronal magnetic field cannot be precisely measured at present except in a few special cases (e.g., Gary & Hurford 1994; Lin et al. 2004), the photosphere (and the chromosphere in a few cases) is the only environment where we can directly observe and measure the magnetic field with sufficient resolutions. In principle, coronal magnetic energy can be derived from photospheric/chromospheric vector magnetograms with the magnetic virial theorem based on a force-free assumption (Molodenskii 1969; Gary et al. 1987; Metcalf et al. 2005). However, the vector magnetic fields measured at the photosphere are quite noisy and are affected by a number of measurement effects, such as systematic crosstalk. The practical application of the virial theorem shows that results are highly sensitive to image noise and systematic errors (Klimchuk et al. 1992).

Another way to estimate the energy budget of active regions is to reconstruct the three-dimensional (3D) coronal field from the measured photospheric boundary based on a force-free assumption. Compared with the virial theorem, field reconstruction imposes a degree of self-consistency that is missing in the virial theorem calculation, and therefore provides a more robust estimate of free energy (McClymont et al. 1997). Reconstructed 3D field also provides a good description of magnetic field topology of active regions (Régner et al. 2002; Wiegelmann et al. 2005; Zhao et al. 2008; Guo et al. 2008; Schrijver et al. 2008; Jing et al. 2008).

With the development of the extrapolation algorithms, the coronal magnetic energy evolution across CME/flare eruptions has been extensively studied. It has been found in general that magnetic energy decreases after solar eruptions, implying that part of magnetic energy is converted into thermal, nonthermal, and kinetic energies of eruptions (e.g., Bleybel et al. 2002; Régner et al. 2002; Régner & Canfield 2006; Guo et al. 2008; Thalmann & Wiegelmann 2008; Thalmann et al. 2008). However, the cadence of the magnetogram observations was generally too low to tell if the drop of the magnetic energy is due to the impulsive energy release in the CME/flare eruptions or merely due to the gradual evolution of the photospheric magnetic field. It was even occasionally found that the magnetic energy increases after the eruptions (e.g., Metcalf et al. 2005), which is probably as a result of the continual pumping of magnetic energy from the subsurface to the corona.

Over the past several years, the Big Bear Solar Observatory (BBSO) has improved its digital vector magnetograph (DVMG) system that achieves a temporal cadence as high as  $\sim 1$  minute and a pixel resolution of  $\sim 0.6$  (Spirock et al. 2002). The field of view (FOV) is up to  $300'' \times 300''$ . As an effort to advance our understanding of CME/flare eruptions, we select four X-class flares and study the temporal variation of free magnetic energy.

As a side remark, for the existing vector magnetographs, there is always a trade-off between polarization precision and temporal and spatial resolution. For example, the spectro-polarimeter (SP) of the Solar Optical Telescope on board the *Hinode* spacecraft is one of the most notable vector magnetographs in operation. It obtains Stokes profiles of two magnetically sensitive Fe lines at 6301.5 and 6302.5 Å. The SP vector magnetograms have advantages in seeing-free, high polarimetric accuracy of 0.1% and very high spatial resolution of  $0.16''$ . But it generally takes a couple of hours to cover a  $164'' \times 164''$  FOV, which is certainly too slow to fulfill our purpose. In comparison, the BBSO/DVMG uses a 0.25 Å filter to measure polarization at only one position in a magnetically sensitive Ca I line at 6103 Å, hence the measurements are generally less accurate than the spectrally resolved measurements due to the Zeeman saturation effect (Lites

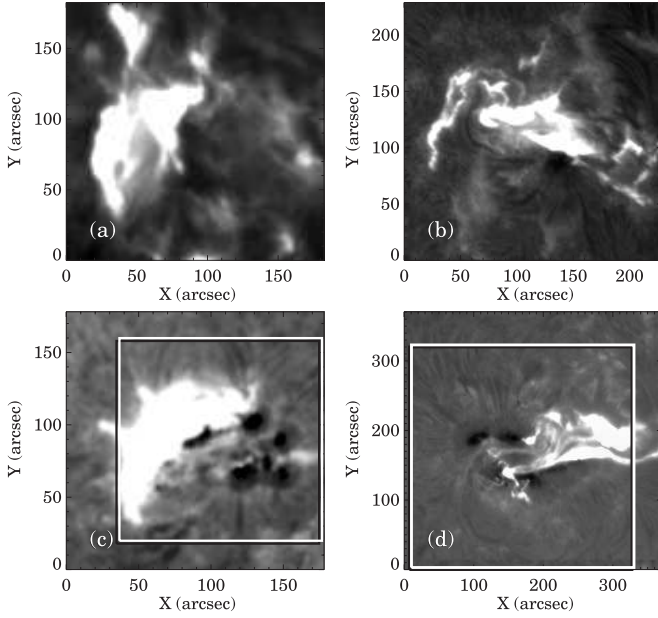


**Figure 1.** Snapshots of the four flares observed in  $H\alpha$ : (a) the X5.3 flare at 16:46 UT, 2001 August 25; (b) the X1.6 flare at 16:30 UT, 2001 October 19; (c) the X1.3 flare at 23:07 UT, 2003 May 27; and (d) the X2.6 flare at 22:50 UT, 2005 January 15. The panels *a* and *b* show the same FOV as the corresponding photospheric vector magnetograms shown in Figures 2(a) and (b). The large square boxes in the panels *c* and *d* mark the FOV of the corresponding magnetograms shown in Figures 2(c) and (d).

et al. 1994). In addition, the DVMG suffers from atmospheric seeing effect. But since the DVMG vector magnetograms are of much higher temporal resolution and good spatial resolution and coverage, it is particularly advantageous to this study as far as we estimate possible errors carefully.

## 2. OBSERVATION AND NONLINEAR FORCE-FREE FIELD EXTRAPOLATION

Figure 1 shows the  $H\alpha$  observations of the four X-class flares studied in this paper. The parameters of the four events are summarized in Table 1. It is noted that all of these flares are not far from the solar disk center, and all of them are associated with halo CMEs.

The vector magnetograms required for this study are obtained by the DVMG system at the BBSO. The DVMG is a filter-based magnetograph that measures photospheric magnetic fields based on weak-field approximation. It consists of a  $0.25 \text{ \AA}$  bandpass filter, a  $1024 \times 1024$  12-bit CCD camera and three liquid crystals used as polarization analyzers. The details of the DVMG hardware are described by Spirock et al. (2002). Each data set includes four data products: Stokes  $I$  (6103  $\text{\AA}$  filtergram), Stokes  $V$  (line-of-sight magnetogram  $B_z$ ), Stokes  $Q$  and  $U$  (transverse magnetograms  $B_x$  and  $B_y$ ). The cadence for a complete set of Stokes images is  $\sim 1$  minute, and the pixel resolution of the rebinned magnetograms is  $\sim 0.6$ . The sensitivity of  $B_z$  and  $B_x$  (and/or  $B_y$ ) is 2 and 20 G, respectively. For each set of magnetograms, the systematic crosstalk between the Stokes  $V$  signal and the  $Q$  and  $U$  signals was corrected by making scatter plots of Stokes  $V$  versus  $Q$  and  $V$  versus  $U$ , respectively. Because the current DVMG system has no mirror in its entire optical path, the instrumental polarization is negligible.

As a filter instrument, the DVMG saturates at field strengths above  $\sim 1000$  G. Those saturated areas appear as voids in the center of sunspots. To reduce the influence of polarization satu-

ration, we use the co-aligned Michelson Doppler Imager (MDI) line-of-sight magnetogram to fill these voids. The  $180^\circ$  azimuthal ambiguity in the transverse magnetograms is resolved using the “minimum energy” algorithm that simultaneously minimizes both the electric current density and the field divergence (Metcalf 1994). This “minimum energy” algorithm is the top-performing automated method among present state-of-art algorithms used for resolving the  $180^\circ$  ambiguity (see Metcalf et al. 2006 for details). The projection effect is corrected for those active regions not near the disk center. Then, we use the DVMG vector magnetograms as the boundary conditions to extrapolate the coronal magnetic fields.

During the past decades, a variety of computational methods have been proposed to extrapolate the nonlinear force-free (NLFF) field, the most general class of force-free field. All these methods are inevitably confronted with the physical problem that the photospheric magnetic field is full of noise and does not satisfy the force-free assumption of extrapolation algorithms. To deal with this problem, Wiegmann et al. (2006) developed a preprocessing procedure that refines the observed nonforce-free data toward suitable boundary conditions for the force-free extrapolation. The preprocessing routine minimizes a functional  $L_{\text{prep}} = \mu_1 L_1 + \mu_2 L_2 + \mu_3 L_3 + \mu_4 L_4$ . The  $L_1$  and  $L_2$  terms contain force-free and torque-free consistency integrals, the  $L_3$  term controls how close the preprocessed data are compared with the original magnetogram (noise level), and the  $L_4$  term controls the smoothing. A strategy on how to choose the parameters  $\mu_i$  was described by Wiegmann et al. (2006). In our cases, the coefficients are taken as  $\mu_1 = \mu_2 = 1$ ,  $\mu_3 = 0.001$ , and  $\mu_4 = 0.01$ . The preprocessing method described above removes the net force and torque from the photosphere boundary, and hence provides an improved input for the subsequent NLFF field extrapolation (Metcalf et al. 2008). For each active region, a set of the DVMG vector magnetograms before and after preprocessing is shown in Figures 2 and 3, respectively.

Schrijver et al. (2006) and more recently Metcalf et al. (2008) quantitatively evaluated the performance of several state-of-art NLFF field extrapolation algorithms in comparison with some analytically known NLFF field solutions. Particularly, the analytical solution used by Metcalf et al. (2008) includes realistic photosphere Lorentz forces and several interesting topological features we expect to see in solar atmosphere, such as a coronal null, a separatrix surface and a S-shape flux bundle. It was found that the optimization algorithm, originally proposed by Wheatland et al. (2000) and implemented by Wiegmann (2004), combined with the preprocessing procedure is the best-performing algorithm in reconstructing the coronal magnetic field.

We then apply the multigrid version of this optimization code to extrapolate the NLFF field from the preprocessed field. Here “multigrid” means that computation is carried out serially on a number of different horizontal grid scales. In our cases, the grid scales, from coarser to finer, are  $25 \times 25 \times 25$ ,  $50 \times 50 \times 50$ ,  $100 \times 100 \times 100$  grid points. The solution from the coarser grids is interpolated into finer grids as the initial state for the next, finer solution. The details of the method were described by Wiegmann (2004) and summarized by Schrijver et al. (2006). In short, this method involves minimizing a joint measure ( $L$ ) for the normalized Lorentz force and the divergence of the field throughout the volume of interest  $V$ :

$$L = \frac{1}{V} \int_V [\omega_f(\mathbf{r}) B^{-2} |(\nabla \times \mathbf{B}) \times \mathbf{B}|^2 + \omega_d(\mathbf{r}) |\nabla \cdot \mathbf{B}|^2] dV, \quad (1)$$

**Table 1**  
Overview of the Flares and the Active Regions

Date	GOES	NOAA	Begin <sup>a</sup> (UT)	Peak <sup>a</sup> (UT)	End <sup>a</sup> (UT)	Location (deg)	CME Association and CME Speed <sup>b</sup> (km s <sup>-1</sup> )
2001 Aug 25	X5.3	9591	16:23	16:45	17:04	S17E34	Halo, 1327
2001 Oct 19	X1.6	9661	16:13	16:30	16:43	N15W29	Halo, 898
2003 May 27	X1.3	10365	22:56	23:07	23:13	S07W17	Halo, 908
2005 Jan 15	X2.6	10720	22:25	23:02	23:31	N15W05	Halo, 2759

**Notes.**

<sup>a</sup> Begin, Peak, End: start, peak and end time of GOES soft X-ray emission.

<sup>b</sup> CME Speed: second-order fit speed provided by SoHO/LASCO CME Catalog.

where  $B = |\mathbf{B}|$ ,  $\omega_f$  and  $\omega_d$  are weighting functions for the force and divergence terms, respectively. The weighting functions  $\omega_f$  and  $\omega_d$  are position-dependent. Both of them are chosen to be 1.0 in the center of the computational box and drop to 0 with a cosine profile in a buffer boundary region that is of 16 grid points toward the side and top boundaries in our cases. The extrapolated NLFF fields of four active regions are shown in Figure 4.

### 3. RESULTS

In this work, the free magnetic energy  $E_{\text{free}}$  of NLFF field is defined as the excess magnetic energy above the potential field, i.e.,

$$E_{\text{free}} = E_N - E_p = \int \frac{B_N^2}{8\pi} dV - \int \frac{B_p^2}{8\pi} dV, \quad (2)$$

where  $V$  is the volume of the computational box, the subscripts  $N$  and  $p$  represent the NLFF field and the potential field, respectively. The latter is computed from the same preprocessed photospheric line-of-sight magnetograms  $B_z$  using a Green's function method (Aly 1989, and references therein). The free energy  $E_{\text{free}}$  calculated in this way is regarded as the upper limit of the energy that is available to power the flares and CMEs.

Figure 5 shows the temporal variation of the free magnetic energy  $E_{\text{free}}$  and the photospheric magnetic flux of the four active regions. The photospheric magnetic flux is calculated by integrating  $B_{\text{rad}}$  over the FOV of the photospheric vector magnetograms, where  $B_{\text{rad}}$  is the radial component of the magnetic field calculated from  $B_x$ ,  $B_y$ ,  $B_z$ . The commencement of the flares is indicated by their nonthermal emissions in either hard X-ray or microwaves that are shown as the gray spiky curves. The main peak of the gray curves can represent the impulsive phase of the solar flares. For each of four events, we apply a Monte Carlo method to one set of observed vector magnetograms  $B_x$ ,  $B_y$ , and  $B_z$  to estimate the uncertainties in  $E_{\text{free}}$  caused by the image noise (see Guo et al. 2008): first, we generate artificial errors for  $B_x$ ,  $B_y$  and  $B_z$ . The errors are in normal distribution with the standard deviation of 2 G for  $B_z$  and 20 G for  $B_x$  and  $B_y$ . The chosen noise levels relate to the sensitivity of the DVMG system. Then, we superimpose the errors to the observed magnetograms and redo the data reduction and NLFF field extrapolation as described in Section 2. We repeat the same process 30 times and calculate the standard deviations of  $E_{\text{free}}$  that is also shown in Figure 5 as error bars.

One particular concern for the results is that how well the free energy  $E_{\text{free}}$  is being reproduced with the NLFF field extrapolation. We are aware of that the use of photospheric, nonforce-free vector magnetogram data, even being preprocessed, may still lead to a systematic underestimate of the free energy (Metcalf

et al. 2008). But this systematic underestimate is unlikely to affect the temporal variation under consideration here, as far as the photospheric magnetograms were obtained under a stable observing condition.

The first impression of Figure 5 is that the evolution of  $E_{\text{free}}$  is synchronous with that of the photospheric magnetic flux, except near the flare occurrence. This is not surprising since the coronal magnetic energy is stored by the changes in photospheric boundary conditions, such as flux emergence, flux cancellation or sunspot motion (Priest & Forbes 2002, and references therein).

We also note that, although long-term trend of  $E_{\text{free}}$  varies from event to event,  $E_{\text{free}}$  ubiquitously shows a decrease  $\sim 15$  minutes prior to the flare peak time. For the first two events (panels a and b), since the start time of the magnetogram observations is only  $\sim 18$  minutes before the impulsive phase of the flares, we cannot follow the magnetic evolution well before the eruptions. But it is evident that both  $E_{\text{free}}$  and the magnetic flux are decreasing during this  $\sim 18$  minute period. For the third and fourth events (panels c and d), the magnetogram observations starts more than  $\sim 50$  minutes before the flares. We see that, well before the flare occurrence,  $E_{\text{free}}$  is steadily increasing in both cases, consistent with the general trend of the magnetic flux evolution. However, at  $\sim 15$  minutes before the flare impulsive phase,  $E_{\text{free}}$  in both cases starts to drop down. The decreasing trend of  $E_{\text{free}}$  as mentioned above is indicated by the green lines. After the flares,  $E_{\text{free}}$  may recover to its increasing trend (e.g., the third event in panel c) or decrease slightly (e.g., the fourth event in panel d).

Again, here  $E_{\text{free}}$  is the excess energy of an NLFF field over the corresponding potential field, and is regarded as the upper limit of the magnetic energy available for the dynamic processes. Not all of  $E_{\text{free}}$  is really free. For this reason, with the relaxation of the NLFF field toward the potential configuration,  $E_{\text{free}}$  became lower after the flares, but not zero.

### 4. DISCUSSION

The phenomena of solar eruptive activity, such as flares and CMEs, correspond to a rapid energy releasing process, where coronal magnetic energy is efficiently converted into the kinetic and thermal energies of the plasma and the nonthermal energy of accelerated particles. The magnetic energy in the corona is accumulated gradually through continual magnetic flux emergence from the subsurface (Zirin 1983), surface motions (including shearing and twisting motions, e.g., McClymont & Fisher 1989, page 219), and low atmospheric reconnection driven by the former two processes (Wang & Shi 1993). As the coronal magnetic configuration becomes more and more complex, the magnetic field is approaching a metastable state. Thereafter, it becomes

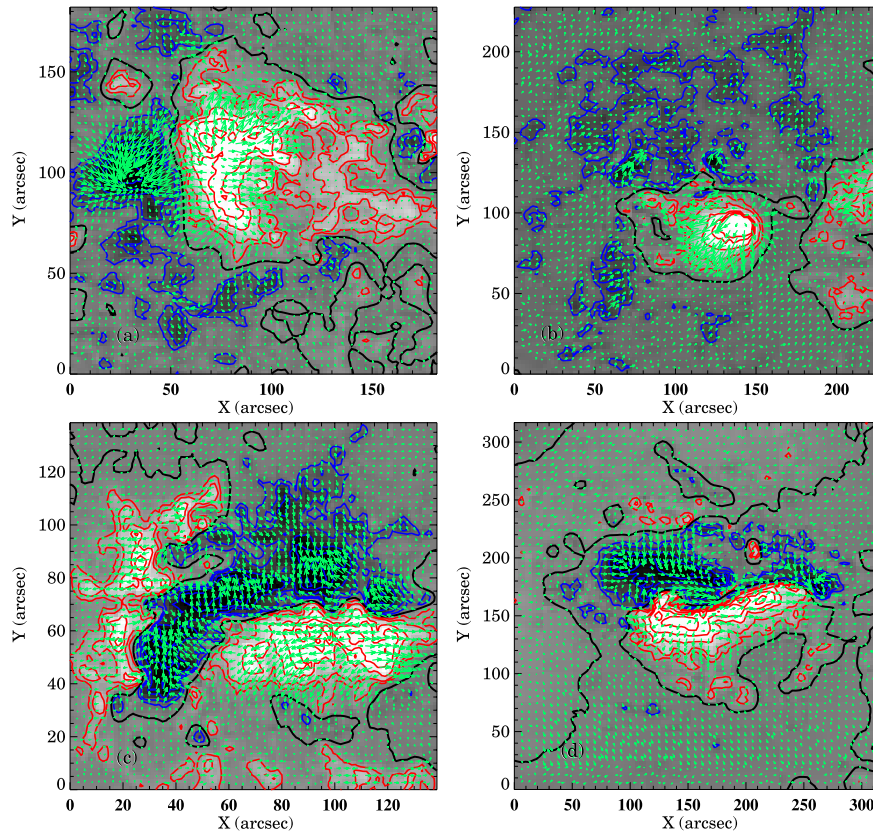


**Figure 2.** Disambiguated vector magnetograms of four active regions: (a) NOAA 9591 taken on 2001 August 25 at 16:26 UT; (b) NOAA 9661 taken on 2001 October 19 at 16:15 UT; (c) NOAA 10365 taken on 2003 May 27 at 22:31 UT; and (d) NOAA 10720 taken on 2005 January 15 at 22:06 UT. The background images are the line-of-sight magnetograms. Green arrows indicate the transverse fields. Red and blue contours are for negative and positive line-of-sight magnetic field strength, respectively. The thick, solid black lines are the magnetic polarity inversion lines.

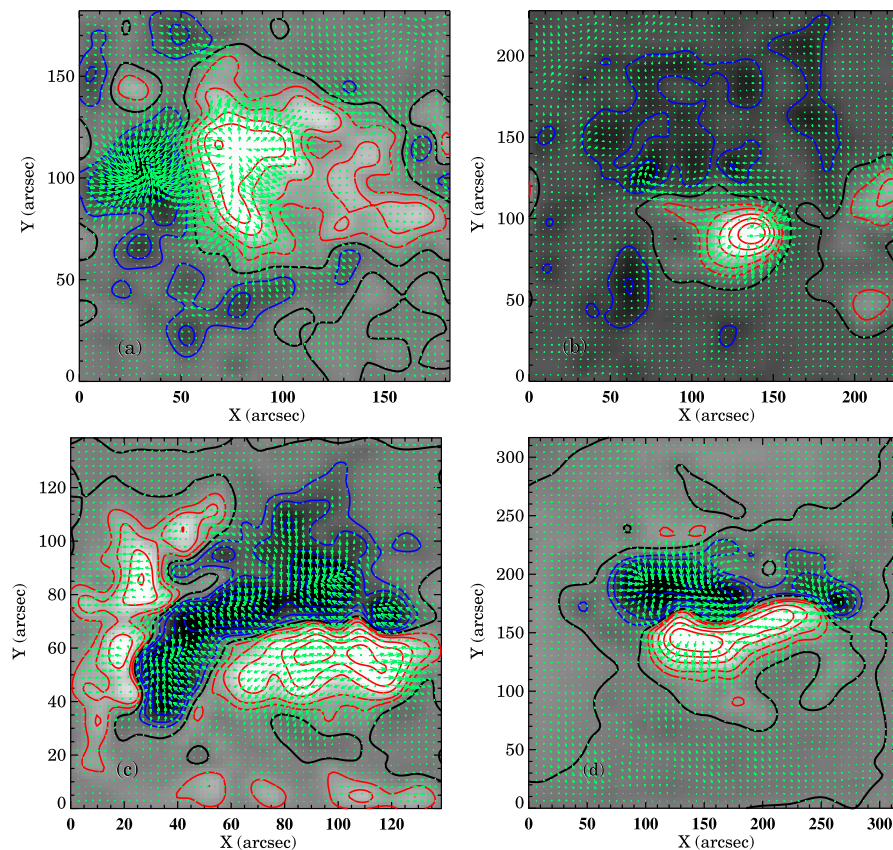


**Figure 3.** As Figure 2, but the vector magnetograms are preprocessed.

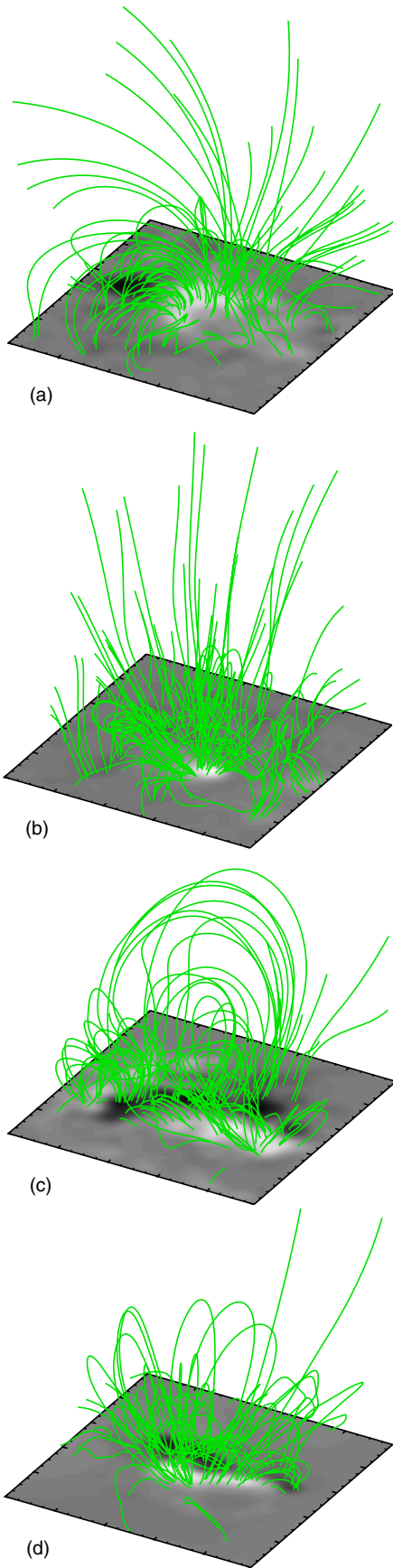


**Figure 4.** Extrapolated NLFF field of four active regions. The panels are in the same order as that in Figures 1–3. The boundary images are the preprocessed line-of-sight magnetograms shown in Figure 3. The dimensions of computation box are: (a)  $185'' \times 185'' \times 185''$ ; (b)  $230'' \times 230'' \times 230''$ ; (c)  $140'' \times 140'' \times 140''$ ; (d)  $320'' \times 320'' \times 320''$ .

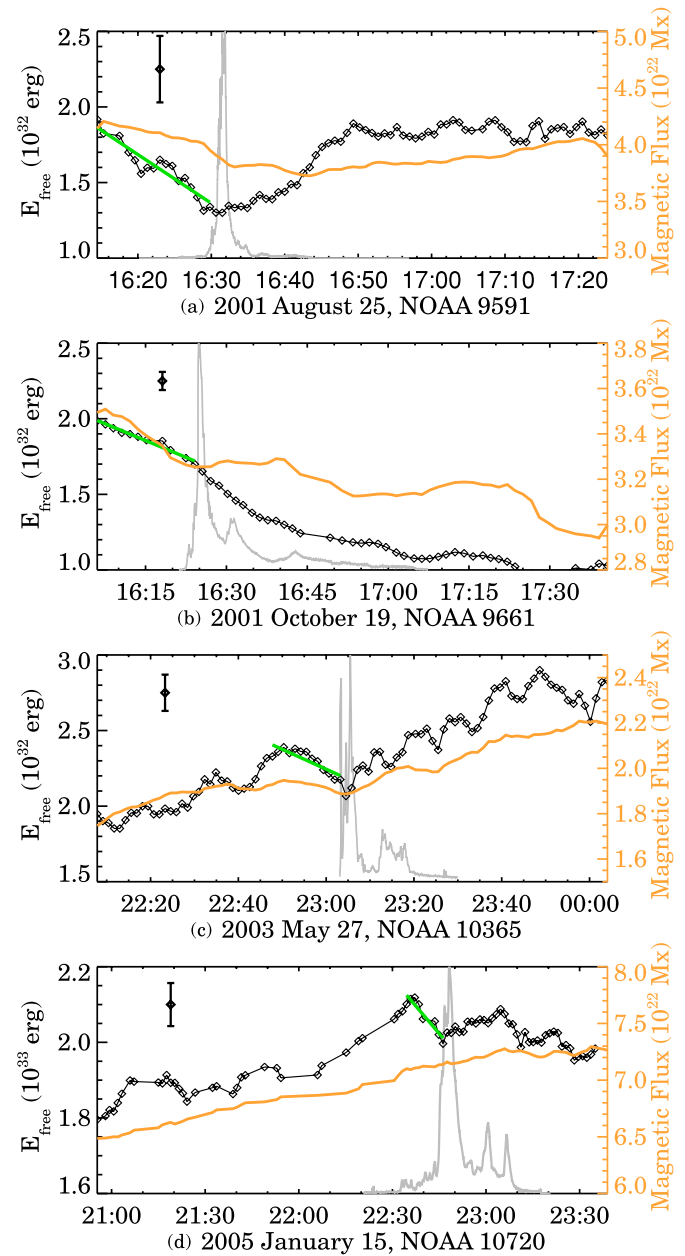


**Figure 5.** Temporal variation of the free magnetic energy  $E_{\text{free}}$  (black diamond) and the photosphere magnetic flux (orange) of four active regions: (a) NOAA 9591 on 2001 August 25; (b) NOAA 9661 on 2001 October 19; (c) NOAA 10365 on 2003 May 27; and (d) NOAA 10720 on 2005 January 15. The gray curves indicate the flare nonthermal emission in arbitrary units. They are Yohkoh hard X-ray light curve in the 53–93 keV H channels (panel a), OVSA microwave 10.0 GHz light curve (panel b), and RHESSI hard X-ray 50–100 keV light curve (panels c and d). The green lines indicate the decreasing trend of  $E_{\text{free}}$   $\sim 15$  minutes prior to the flares. The error bars indicate the uncertainties in  $E_{\text{free}}$ .

unstable or close to loss of equilibrium, and it is ready to be triggered to erupt by further emerging flux or surface motions. Free magnetic energy is released partly to power solar flares and CMEs. Since the details in observations and physics are far from being fully understood, it would be crucial to scrutinize the evolution of the source active regions. Multiwavelength radiative signatures of the CME/flare initiations were extensively studied (e.g., Wang et al. 2000; Chen et al. 2008, and references therein), while the physical understanding of these observational precursors inevitably involves the magnetic structure in the corona, which, on the other hand, can directly be inferred from photo-

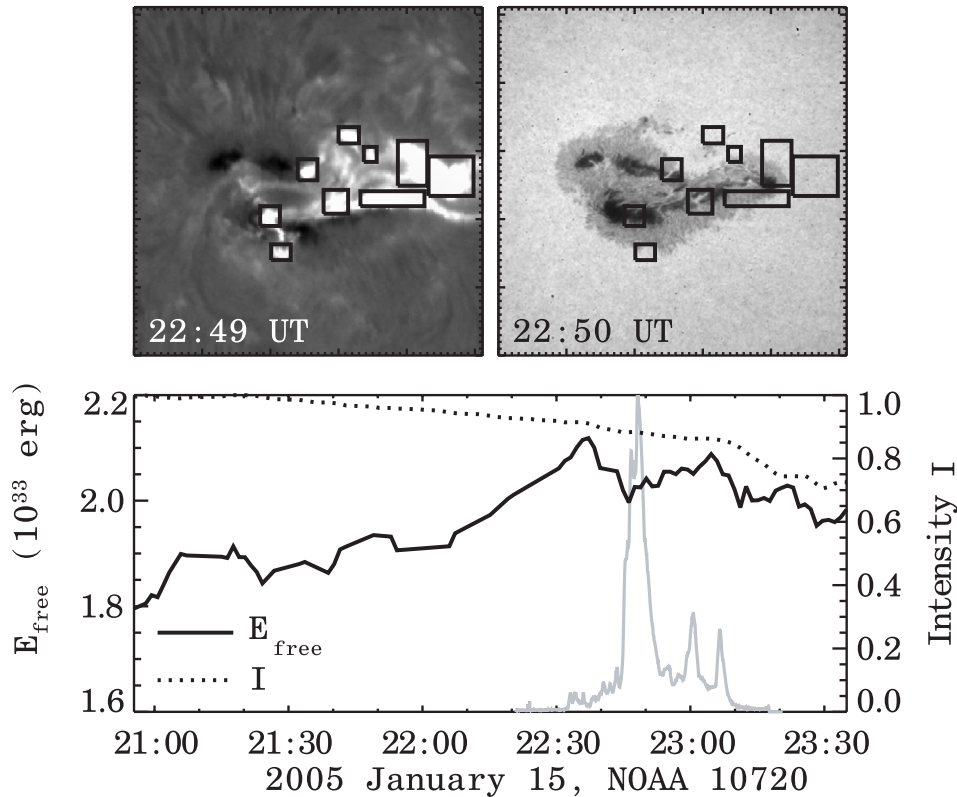


**Figure 6.** Top panels: the BBSO H $\alpha$  image (left) and the DVMG filtergram (right). The rectangular boxes mark the most prominent flaring regions. Bottom panel: time variation of the free magnetic energy  $E_{\text{free}}$  (solid black curve) and the mean filtergram intensity  $I$  (dotted curve) in the rectangular regions for the 2005 January 15 event.  $I$  is normalized to its maximum. The gray curve is the RHESSI hard X-ray 50–100 keV light curve in arbitrary units.

spheric magnetograms. The properties of the coronal magnetic field, such as free energy, helicity, and so on, can be analyzed in order to understand the CME/flare initiations.

However, evaluating the coronal free magnetic energy from the photospheric vector magnetogram data is a complex task, primarily because that the observable photospheric field is intrinsically inconsistent with the force-free assumption. With the preprocessing method developed by Wiegelmann et al. (2006) and the reliable NLFF field extrapolation algorithm implemented by Wiegelmann (2004), we are able to study the evolution of the free magnetic energy across CME/flare eruptions. The 1 minute cadence BBSO/DVMG vector magnetogram data further enable us to trace the coronal magnetic evolution in a high time resolution.

In all the four strong CME/flare events, we find that the coronal free energy starts to drop evidently at least  $\sim 15$  minutes before the impulsive phase of the associated flare. Such a result suggests that the coronal magnetic structure is already triggered to relax before the occurrence of flare-associated magnetic reconnection. The relaxation of the strongly twisted coronal magnetic field corresponds to the CME initiation, which is characterized by the expansion and untwisting of twisted coronal loops. Around 15 minutes before the flare occurrence, the untwisting of coronal field lines is transferred to the photosphere, making the vector magnetograms less sheared (this is why the extrapolated free magnetic energy starts to decrease). Such a result is also consistent with the following paradigm for CME/flare eruptions (e.g., see Zhang et al. 2001 for observations and Chen & Shibata 2000 for MHD simulations): a metastable coronal structure is triggered to rise, along which the strongly twisted coronal loops are

expanding as well as untwisting. As the coronal loops expand, a current sheet forms above the magnetic neutral line (presumably below a flux rope). The reconnection of the current sheet leads to the rapid eruption of a CME and an associated flare.

Another striking feature of Figure 5 is that, in three events (panels a, c, and d), the decrease of  $E_{\text{free}}$  terminates after the hard X-ray peak. Only in the second event (panel b),  $E_{\text{free}}$  continues to decline even after the hard X-ray peak, which is probably due to the decay of the magnetic field as indicated by the time variation of the magnetic flux (orange line).

It has been reported that the measurements of magnetic fields may be distorted temporarily during strong flares as a result of the prominent nonthermal impact on the photospheric atmosphere. Such a transient magnetic field change is referred to as “magnetic transient” (Patterson & Zirin 1981; Kosovichev & Zharkova 2001) or “magnetic anomaly” (Qiu & Gary 2003). We note that, in the first three events (panels a, b, and c), the decreasing trend of  $E_{\text{free}}$  occurs well before the onset of the flares. However, in the fourth event (panel d), as  $E_{\text{free}}$  suddenly deviates from the increasing trend and begins decreasing, RHESSI light curve (gray line) indicates weak nonthermal emissions. Hence, there is another possibility that the observed energy drop in the fourth event might be due to the distortion of the magnetic measurements during the nonthermal heating of the photospheric atmosphere. In order to check this issue, Figure 6 shows the time variations of  $E_{\text{free}}$ , the mean Stokes  $I$  (i.e., the mean filtergram intensity) in the most prominent flaring regions that are marked by the rectangular boxes, and the hard X-ray (50–100 keV) intensity. Evidently, the filtergram intensity  $I$  is not subject to the impact of the nonthermal emission. In other

words, the energy drop during the preflare phase is not caused by the transient nonthermal effects, but ascribed to the real changes in the magnetic field.

We also note that the free magnetic energy may even increase after flares, as indicated by the third event (panel c of Figure 5). This is probably due to the continual pumping of magnetic field from subsurface to the corona, as implied by the continual increase of the magnetic flux, and/or the increase of the magnetic shear. This reminds us that high cadence magnetogram observations are necessary when we study the magnetic energy variation associated with the CME/flare eruptions. In this sense, it is worth mentioning that the Solar Dynamic Observatory (SDO) is expected to be launched in 2009. The Helioseismic and Magnetic Imager (HMI) on board the SDO will be the first instrument to provide routine measurements of the full-disk photospheric vector magnetogram data with high spatial and temporal resolution under seeing-free condition. We anticipate extending the current study with the upcoming SDO/HMI vector magnetograms.

We thank Chang Liu for providing hard X-ray light-curve data. J.J. and H.W. were supported by NSF under grant ATM 07-16950, ATM 05-48952 and NASA under grant NNX0-7AH78G and 8AQ90G. T.W. was supported by DLR-grant 50 OC 0501. P.F.C. was supported by the Chinese foundations GYHY200706013, 2006CB806302, and NSFC (10403003).

#### REFERENCES

- Aly, J. J. 1989, *Sol. Phys.*, **120**, 19
- Bleybel, A., Amari, T., van Driel-Gesztelyi, L., & Leka, K. D. 2002, *A&A*, **395**, 685
- Chen, P. F., Innes, D. E., & Solanki, S. K. 2008, *A&A*, **484**, 487
- Chen, P. F., & Shibata, K. 2000, *ApJ*, **545**, 524
- Gary, D. E., & Hurford, G. J. 1994, *ApJ*, **420**, 903
- Gary, G. A., Moore, R. L., Hagyard, M. J., & Haisch, B. M. 1987, *ApJ*, **314**, 782
- Guo, Y., Ding, M. D., Wiegelmann, T., & Li, H. 2008, *ApJ*, **679**, 1629
- Jing, J., Wiegelmann, T., Suematsu, Y., Kubo, M., & Wang, H. 2008, *ApJ*, **676**, L81
- Klimchuk, J. A., Canfield, R. C., & Rhoads, J. E. 1992, *ApJ*, **385**, 327
- Kosovichev, A. G., & Zharkova, V. V. 2001, *ApJ*, **550**, L105
- Lin, H., Kuhn, J. R., & Coulter, R. 2004, *ApJ*, **613**, L177
- Lites, B. W., Pillet, V. M., & Skumanich, A. 1994, *Sol. Phys.*, **155**, 1
- McClymont, A. N., & Fisher, G. H. 1989, *Solar System Plasma Physics: Geophysical Monograph 54*, ed. J. H. Waite, Jr, J. L. Burch, & R. L. Moore (Washington, D.C.: American Geophysical Union)
- McClymont, A. N., Jiao, L., & Mikić, Z. 1997, *Sol. Phys.*, **174**, 191
- Metcalf, T. R. 1994, *Sol. Phys.*, **155**, 235
- Metcalf, T. R., Leka, K. D., & Mickey, D. L. 2005, *ApJ*, **623**, L53
- Metcalf, T. R., et al. 2006, *Sol. Phys.*, **237**, 267
- Metcalf, T. R., et al. 2008, *Sol. Phys.*, **247**, 269
- Molodenskii, M. M. 1969, *SvA*, **12**, 585
- Patterson, A., & Zirin, H. 1981, *ApJ*, **243**, L99
- Priest, E. R., & Forbes, T. G. 2002, *A&AR*, **10**, 313
- Qiu, J., & Gary, D. E. 2003, *ApJ*, **599**, 615
- Régnier, S., Amari, T., & Kersale, E. 2002, *A&A*, **392**, 1119
- Régnier, S., & Canfield, R. C. 2006, *A&A*, **451**, 319
- Schrijver, C., et al. 2006, *Sol. Phys.*, **235**, 161
- Schrijver, C., et al. 2008, *ApJ*, **675**, 1637
- Spirock, T., Yurchyshyn, V. B., & Wang, H. 2002, *ApJ*, **572**, 1072
- Thalmann, J. K., & Wiegelmann, T. 2008, *A&A*, **484**, 495
- Thalmann, J. K., Wiegelmann, T., & Raouafi, N. E. 2008, *A&A*, **488**, L71
- Wang, J., & Shi, Z. 1993, *Sol. Phys.*, **143**, 119
- Wang, H., et al. 2000, *ApJ*, **536**, 971
- Wheatland, M. S., Sturrock, P. A., & Roumeliotis, G. 2000, *ApJ*, **540**, 1150
- Wiegelmann, T. 2004, *Sol. Phys.*, **219**, 87
- Wiegelmann, T., Inhester, B., Lagg, A., & Solanki, S. K. 2005, *Sol. Phys.*, **228**, 67
- Wiegelmann, T., Inhester, B., & Sakurai, T. 2006, *Sol. Phys.*, **233**, 215
- Zhang, J., Dere, K. P., Howard, R. A., Kundu, M. R., & White, S. M. 2001, *ApJ*, **559**, 452
- Zhao, H., Wang, J. X., Zhang, J., Xiao, C. J., & Wang, H. M. 2008, *Chin. J. Astron. Astrophys.*, **8**, 133145
- Zirin, H. 1983, *ApJ*, **274**, 900